Dynamic characterization of wall temperature in LOX/CH 4 rocket engine operating conditions using phosphor thermometry

Valentin Lechner, Christopher Betrancourt, Philippe Scouflaire, Lucien Vingert, Sebastien Ducruix

Dynamic characterization of wall temperature in LOX/CH_4 rocket engine operating conditions using phosphor thermometry

V. Lechner[a,b,*], C. Betrancourt[b], P. Scouflaire[b], L. Vingert[c], S. Ducruix[b]

[a] *CNES, Direction Technique et Numérique, Paris, France*
[b] *Université Paris-Saclay, CNRS, CentraleSupélec, Laboratoire EM2C, Gif-sur-Yvette, France*
[c] *DMPE, ONERA, Université Paris-Saclay, Palaiseau, France*

Abstract

Accurate surface temperature prediction is essential for the lifetime and efficiency of a rocket engine. The new ambition of future reusable engines requires perfect knowledge of the thermal environment encountered. In the design phase of such systems and to improve numerical simulations, more resolved experimental data are needed. Experiments are thus conducted by Lab. EM2C, ONERA, CNES, and ArianeGroup on the cryotechnic test bench MASCOTTE operated by ONERA. Conditions representative of those encountered in the gas generator of a rocket engine are investigated. Among them is the cryogenic injection of transcritical methane and oxygen at a very low mixture ratio (0.3) and high pressure (up to 60 bar) through a single coaxial injection element. The present work aims at characterizing the temperature of several surfaces of the combustion chamber in a series of hot fire tests performed in the transient thermal regime and in a short period of time ($\sim$30 s). For this purpose, dynamic Laser Induced Phosphorescence (LIP) is implemented with the Full Spectrum Fitting method (FSF method), a dedicated approach developed by Lab. EM2C. Single-shot measurements are performed to simultaneously track the temperature of five surfaces at 10 Hz located near and downstream of the flame with a 30 K uncertainty. Data indicate that the temperature peak at ignition can be recorded with LIP measurements in contrast to conventional sensors. The analysis of gas and surface temperatures shows that convection is the predominant heat transfer mode and drives the surface temperature. Thanks to LIP thermometry on the internal and external faces of one of the silica windows, a 1D semi-infinite medium model is applied, showing excellent agreement with the measurements. Fitting this model on the measurements allows the estimation of the local convection coefficient and the prediction of the temperature at any depth inside the walls.

Keywords: Surface thermometry; Instantaneous measurements; Transcritical combustion

1. Introduction

Facing international competition, a new generation of reusable European launchers needs to be developed. In order to select the best candidate for their propulsion, possibly equipping both upper and lower stages, technological demonstration activities are performed in the frame of ESA Future Launchers Preparatory Program (FLPP). Propulsion could be provided by liquid rocket engines using liquid oxygen (LOX) and methane (CH_4). In-flight re-ignition, thrust throttling, and re-usability are some of the main objectives of these new cost-effective engines.

As thermal loads can reach up to 200 $MW{\cdot}m^{-2}$ on the combustion chamber wall of a rocket engine [1], understanding and predicting the different heat transfer mode contributions is mandatory for the development of a reusable engine. Creep prediction and life cycle highly depend on the accuracy of wall temperature prediction. Moreover, the wall temperature can trigger transitions between different flame topologies [2]. This coupling could be retrieved by Large Eddy Simulations (LES), by taking into account precise thermal boundary conditions directly measured on the walls of a laboratory scale burner [3].

During the inaugural launch of the ECA version of Ariane 5 (flight 517), a failure of the Vulcain engine caused the loss of the mission [4]. A wrong estimation of the thermal constraints on the nozzle extension hot side led to reduced mechanical margins. Associated with other causes, this led to the critical buckling of the nozzle extension.

The extreme thermal conditions encountered in a rocket engine make the design work of such chambers highly complex. More accurate and time-resolved experimental surface temperature measurements are needed to improve the heat transfer prediction in representative rocket engine operating conditions: ignition, thrust stabilization, and thrust throttling.

These challenges are tackled within the Lab. EM2C / ONERA / CNES / ArianeGroup R&D consortium through investigations conducted at the MASCOTTE test bench [5], an experimental setup operated by ONERA equipped with a single coaxial injection element and reproducing similar operating conditions as reached in rocket engines. Advanced diagnostics are implemented simultaneously to understand the behavior of LOX/CH_4 cryogenic flames at a low mixture ratio and when propellants are injected in either transcritical or liquid thermodynamic states. Among them, dynamic Laser Induced Phosphorescence (LIP) thermometry measurements are performed for the first time on this bench.

LIP is an established optical method to measure surface temperature [6]. A thermographic phosphor coating is applied on surfaces of interest. A phosphorescence signal is emitted under laser irradiation which temporal and spectral properties are temperature-dependent. These properties are used to determine an unknown temperature through an appropriate calibration.

LIP has been extensively used to characterize the surface temperature and so the heat flux in laboratory combustors operating in steady thermal regimes [7–9]. High-speed thermometry is required for measurements in short transient thermal regimes [10, 11], while few applications on full-scale engines are reported in the literature. For example, measurements were performed at the exhaust stream [12] and directly on the outlet nozzle of a turbojet afterburner [13] or recently inside a gas turbine combustor at 8 bar [14].

On the MASCOTTE test bench, experiments are performed in the transient thermal regime because the operation duration does not exceed $\sim$30 s due to the extreme conditions reached. Single-shot measurements are thus required to track the unsteady evolution of temperature and the intense heat flux at the ignition.

The so-called "Full Spectrum Fitting method" (FSF method) has been developed by Lab. EM2C [15] for measurements in such harsh environments. The FSF method consists in a new post-processing and spectral approach of the LIP signal. Using the phosphor $Mg_{3.5}FGeO_5$:Mn, single-shot measurements can be performed in a temperature range from 100 K to 900 K with a unique set of experimental acquisition parameters [15].

The present work highlights the first use of dynamic phosphor thermometry in rocket engine conditions. The dynamic temperature of five surfaces of the combustion chamber is tracked simultaneously during hot fire tests thanks to the FSF method.

2. Experimental setup

2.1. MASCOTTE cryotechnic bench

Experiments are conducted in the BHP combustion chamber on the cryotechnic test bench MASCOTTE operated by ONERA at their Palaiseau center [5]. Figure 1 shows the main components of this mono-injection element chamber composed of modules of 50×50 mm^2 section. Two visualization modules are used simultaneously for optical accesses directly to the injection exit and downstream of the flame, in a zone of burnt gases. The first module has three optical accesses with silica windows (Corning 7980) of 45 mm thickness. The fourth location, at the top, is occupied by a blind window fitted with the H_2/O_2 ignition torch and a pressure sensor (Kulite). Two optical accesses are available in the second visualization module.

Methane and oxygen are injected through the injection head and a single coaxial injection element. The oxygen is fed by a central tube (LOX post), and the methane by an outer tube. Two versions of this injection element are used, with (WR) and without recess (NR) of the LOX post.

The mixture ratio, $MR = \dot{m}_{O_2}/\dot{m}_{CH_4}$, is kept constant at 0.3. Oxygen and methane are injected at constant temperatures of 110 K and 140 K respectively.

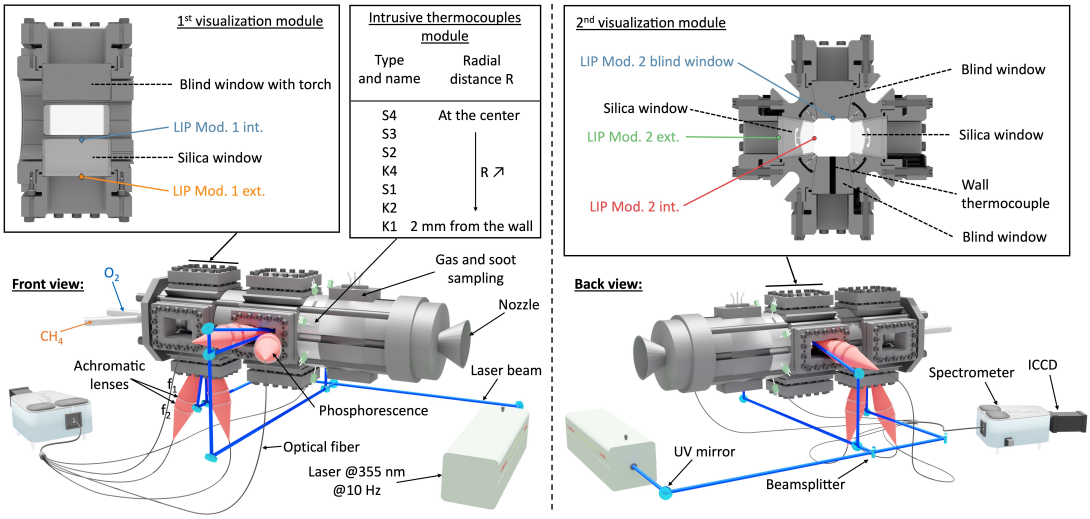

Fig. 1: BHP combustion chamber, phosphor thermometry experimental setup, and locations of LIP measurements. Illustration not at scale.

Three chamber pressures are targeted to reach both subcritical injections (26 bar), a combination of subcritical O_2 and transcritical CH_4 injections (48 bar), and both transcritical injections (60 bar). Changing propellants mass flow rates and a copper converging-diverging nozzle define these operating pressures. The flame is ignited by the H_2/O_2 torch.

Six operating points are thus defined with three targeted pressures and two injection element geometries. They are designated as the combination of the injection element geometry (WR or NR) and chamber pressure (P26, P48, or P60).

Ungrounded sheathed thermocouples of 2 mm diameter are inserted radially inside the combustion chamber in a vertical plane at 400 mm from the injection plate. Their names, type, and radial positions are indicated in figure 1. Due to radiative transfers between them and the combustion chamber walls, a correction is applied to determine the real temperature of the gas phase. The procedure is detailed in the section 3.2.2. A J-type thermocouple measures the surface temperature in the 2nd visualization module. It is inserted in the bottom blind window and is denoted "wall thermocouple". Blind windows material is stainless steel 314. Signals are acquired at 100 Hz.

2.2. *Phosphor thermometry*

The coating is obtained by mixing $Mg_{3.5}FGeO_5$:Mn phosphor powder (Phosphor Technology, EQD25/NU1) with a commercial binder (ZYP Coatings, HPC Binder) and water. A dilution water volume corresponding to 10% of the binder volume is added. This mixture is coated with an airbrush (Aerograph Services, Utopia C05) with ten layers. Each layer is dried at ambient air conditions for a few minutes. The coated surfaces are finally cured in oven at ∼480 K for 2 hours. The thickness is estimated not to exceed 100 µm. As seen in figure 1, two measurements are performed in the first visualization module and three in the second module. In the first and second modules, silica windows are coated on the internal and external sides. The fifth coating is applied on a blind window in the second module. Each measurement is performed in the middle of the windows.

The coating is exposed to hot gases and high shear stress at elevated pressures during the hot fire tests. Erosion happens over time during the flame ignition, especially on the silica windows with the smoothest surfaces. That is why a relatively thick coating was preferred. However, no change in the phosphorescence signal properties has been observed.

The coated surfaces are excited at 355 nm using the 3rd harmonic of a pulsed Nd:YAG laser (Continuum, Surelite SL II-10) triggered at 10 Hz with a 5 ns width pulse. The laser beam is distributed to the five locations with beamsplitters leading to a 64 mJ·cm^{-2} fluence at each measurement site, for which the illuminated spot size is about 7 mm.

Telescopes are used to collect phosphorescence signals. They are composed of two-inch achromatic lenses ($f_1 = 150$ mm and $f_2 = 100$ mm, Thorlabs, AC508-150-A, and AC508-100-A). The light is then focused on a 200 µm multimode optical fiber (CeramOptec, customed). With a 1.5 magnification, the phosphorescence signal is collected from a 300 µm diameter surface. All fibers are joined in a bundle and are aligned vertically, leading to the entrance slit of a spectrometer (Princeton Instrument, Spectra Pro 500i, $f = 500$ mm, grating of 150 grooves mm^{-1}). One "blind" fiber is added between each "active" fiber to avoid cross-talking. Phosphorescence signals are imaged at 10 Hz with the spectrometer coupled with

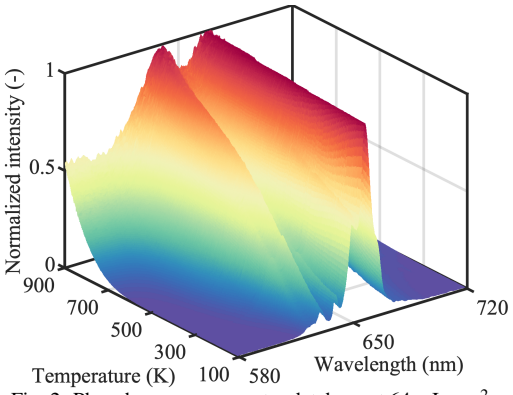

Fig. 2: Phosphorescence spectra database at 64 mJ·cm^{-2}.

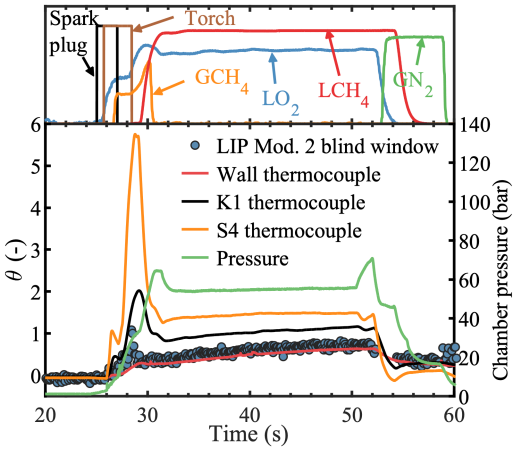

Fig. 3: Top plot: chronograph of an automatic sequence at WRP60 operating point. Bottom plot: temporal evolution of chamber pressure, gas and wall temperatures measured by thermocouples, and LIP measurements on the blind window.

an intensified CCD camera (Princeton Instrument, PiMax, 512 × 512 pixel^2) covering a spectral range of 160 nm centered at $\lambda = 650$ nm with a resolution of 0.3 nm·pixel^{-1}. A 50 ns delay between the laser pulse and the camera exposition is set to avoid any laser contribution and prevent potential interferences from fluorescence sources. The exposure time is set to 30 µs. No interfering signal from the flame has been observed. Each single-shot spectrum is corrected from the dark current and smoothed with a 3-order Savitzky-Golay filter with a moving window of 13 points.

2.3. Calibration and data evaluation

LIP calibration was carried out previously in Lab. EM2C by building databases of phosphorescence spectra at each kelvin from 100 K to 900 K, and laser fluences from 11 to 106 mJ·cm^{-2} at atmospheric pressure. Figure 2 shows an example of a database at 64 mJ·cm^{-2}. The phosphor $Mg_{3.5}FGeO_5$:Mn was chosen for its good spectral dynamics on a wide range of temperatures. Its phosphorescence signal lifetime is about a few milliseconds at ambient temperature compared to a few microseconds at 900 K [8].

The Full Spectrum Fitting method (FSF method) is applied to determine the temperature from the single-shots acquired. A least mean square algorithm is used to find the best agreement between each measured spectrum and one from the database. All the databases at different laser fluences are checked with this procedure leading to the final targeted temperature. Note that the calibration is performed at discrete temperatures at each kelvin. There is no interpolation between the spectra in the databases.

Compared to the established Intensity Ratio method, this post-processing approach allows being nearly independent of the excitation energy, which can be lower than the calibration one in this high-absorbing environment [15]. Moreover, performing dynamic measurements over a wide temperature range involves four orders of magnitude in terms of phosphorescence lifetime and a detector with fast-changing settings or a high dynamic range at a given set. Automatic routines have been imagined [8, 16] but limit the sampling rate to a few hertz, limiting the ability to track transient thermal regimes. Therefore, the FSF method has been developed for these harsh conditions and short durations (∼30 s).

The uncertainty associated with LIP measurements results from different sources. First, the accuracy of the thermocouple used for the calibration adds the fabrication tolerance, ±3 K, and the static error, from ±3 K at 300 K to ±6 K at 800 K. A statistical study performed on thousands of single-shot measurements showed that the precision of the FSF method is ±17 K regardless of the temperature and the excitation energy [15]. Considering a moderate safety coefficient, the uncertainty of LIP measurements in MASCOTTE conditions is finally estimated at ±30 K.

In this work, temperatures are presented in the normalized form θ, using a reference temperature T_{ref}.

3. Results and discussion

3.1. Test sequence analysis

The chronograph of an automatic sequence at WRP60 operating point and the evolution of temperatures and chamber pressure as a function of time are shown in figure 3. The first temperature rise, at $t = 26$ s, corresponds to the ignition of the premixed H_2/O_2 torch flame and is not identified on surface measurements. However, two seconds later, another temperature peak, broader and greater, is captured by phosphor thermometry. Gaseous methane being temporarily injected through the injection element, the mixture ratio is higher than targeted with liquid methane for almost two seconds. Temperatures then decrease as pure liquid methane is being injected. From ignition up to $t = 32$ s, the pres-

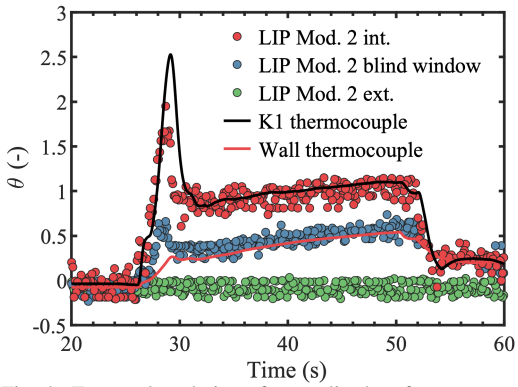

Fig. 4: Temporal evolution of normalized surface temperatures in the 2nd visualization module and measured by K1 thermocouple at WRP48 operating point.

sure slowly increases with the increase of mass flow rates. Starting at $t = 32$ s, when oxygen and methane mass flow rates reach targeted values, the temperature of burnt gases (S4 thermocouple) almost reaches a steady-state up to the extinction except for the thermocouple K1, the closest to the wall, for which the temperature increases during the whole run like for surface measurements. It should be noted that the BHP is an uncooled chamber that functions as a heat sink, which explains why the wall temperature continues to increase. The extinction starts at $t = 52$ s, by decreasing the oxygen mass flow rate, leading to a lower mixture ratio and lower temperatures. Pressure and temperatures finally strongly decrease with the flame extinction and during a purge by gaseous nitrogen to avoid any detonation or backfire. The two pressure peaks at the beginning and end of the run correspond to the injection of gaseous helium near silica windows to protect them from the strong heat flux variations. These observations are identical at the two other pressure conditions.

3.2. Heat transfer modes analysis

3.2.1. Inside the phosphor coating

Figure 3 shows that the temperature near the walls still increases during the steady state of a hot fire test. The BHP combustion chamber walls are thus transient systems. Temperature gradients may appear inside the phosphor coating: the side in contact with the surface and the one exposed to the environment may be at different temperatures. This may lead to errors of up to 100 K [17, 18].

The coating thickness remains the critical parameter regarding conduction transfers [18], so thin coatings are preferred. The Biot and Fourier numbers are now estimated to evaluate the importance of temperature gradients within the coating:

$$Bi = \frac{he}{\lambda}, \qquad Fo = \frac{at}{e^2}, \tag{1}$$

with h the convection coefficient, e the coating thickness (100 µm), λ the thermal conductivity, a the thermal diffusivity, and t a given time. The thermal properties of phosphor coatings are not well-documented but may be similar to those of the binder used, which is the main component of the coating. This binder is composed of magnesium aluminum silicate which conductivity is $\lambda = 2.2\,\mathrm{W{\cdot}m^{-1}{\cdot}K^{-1}}$ and diffusivity is $a = 0.014\,\mathrm{cm^2{\cdot}s^{-1}}$.

Evaluating the convection coefficient h is not straightforward in these conditions so that a rough estimation is made in the following part. In the 2nd module, thermal properties are evaluated at the film temperature $\theta = 0.95$ and at 60 bar, assuming that methane is the main component of the burnt gases. Reynolds and Prandtl numbers are evaluated from the total mass flow and the hydraulic diameter (50 mm). These values are then used to determine the Nusselt number $Nu = he/\lambda_{gas}$ from the Ditus correlation $Nu = 0.0296 Re^{4/5} Pr^{1/3}$. One then obtains a first estimation of the convection coefficient value: $h_{est} = 736\,\mathrm{W{\cdot}m^{-2}{\cdot}K^{-1}}$. Finally, this gives a Biot number of 0.033, meaning that the conduction time inside the coating is shorter than the convection time in the coating boundary. Besides, from $Fo = 1$, $t = e^2/a$ gives a characteristic diffusion time of 7 ms, which is smaller than the period of LIP signals acquisition. The temperature can thus be considered as homogeneous in the phosphor coating.

Note that using thick coatings in other conditions requires assessing the penetration of the laser and the phosphorescence generation to estimate thermal gradients [19], especially when the coating is excited in the back of the silica windows.

3.2.2. Downstream of the flame

An example of the surface temperatures in the 2nd visualization module at WRP48 operating point is shown in figure 4. LIP measurements on the blind window are in good agreement with the ones from the wall thermocouple. One critical phenomenon captured by LIP measurements is the temperature peak at $t = 28$ s due to a higher mixture ratio during the injection of gaseous methane. It is not well-captured and delayed by the wall thermocouple whose response time (∼300-500 ms) is longer. LIP measurements may not give the proper temperature peak because of the acquisition at 10 Hz. Still, single-shot measurements allow detecting the temperature dynamics during a hot fire test, which would not be possible with LIP average signals. The wall thermocouple systematically underestimates the temperature peak after ignition for all operating points.

The internal temperature of the silica window (Mod. 2 int.) is very close to the one measured by thermocouple K1. However, the temperature peak measured by LIP is lower on the window and the one measured by the thermocouple is delayed, again due to a slower response time of a few tenths of a second. From the thermal properties in table 1 and

Table 1: Windows thermal properties at 298 K.

Material	λ (W·m^{-1}·K^{-1})	a (cm^2·s^{-1})
Silica corning 7980	1.3	0.0075
Stainless steel 314	15.0	0.038

$h = h_{est} = 736\,\mathrm{W{\cdot}m^{-2}{\cdot}K^{-1}}$, one obtains $Bi > 1$ for both the silica and blind window. It means that the conduction time is larger than the characteristic time of convection and that the difference between the body surface temperature and the fluid temperature in its thermal boundary layer becomes negligible.

The estimated convection coefficient can be used to correct the thermocouple values from the radiative losses between them and the combustion chamber walls. Assuming a transparent gas, the thermocouple energy balance equation is composed of the convective transfer, the emitted and the absorbed radiations

$$h(T_g - T) + \epsilon\sigma(T_w^4 - T^4) = 0, \qquad (2)$$

with T_g the real gas temperature, T the temperature given by the thermocouple (S4), ϵ the emissivity of the thermocouple considered as a gray body, σ the Stefan constant, and T_w the temperature of the surrounding wall measured by LIP. Conductive transfers inside the thermocouple are not considered due to the high thermal conductivity of the ceramic used, typically magnesium oxide. The surface temperature of the thermocouple is thus considered as the measuring junction one. At WRP48 operating point, with 0.8 for the emissivity and $h = h_{est} = 736\,\mathrm{W{\cdot}m^{-2}{\cdot}K^{-1}}$, the temperature difference is about 15 K at $t = 40$ s. This confirms again the predominant effect of convection in this zone of the combustion chamber. The final thermocouples correction is determined thanks to the procedure described in the following paragraphs.

The thermal properties differences of silica and stainless steel 314 can explain the different evolution of the internal temperatures. One can make the hypothesis that they can be modeled as semi-infinite media. A medium is considered semi-infinite when one of its faces does not respond to a thermal perturbation applied on the opposite face. As seen in figure 4, there is no increase of the temperature in the external face of the silica window. This is true for all operating points. Yet, the semi-infinite medium model only has a physical meaning when the thickness of the medium verifies $e >> \sqrt{at}$. Considering a maximum run time of 25 s, one obtains $\sqrt{at} = 4.33$ mm for the silica window and $\sqrt{at} = 9.75$ mm for the blind window, below the 45 mm thickness. The hypothesis of the semi-infinite medium is thus acceptable during such a short hot fire test. Moreover, one can assume that these media are subjected to an imposed and constant convection coefficient h. With z the thickness direction, the energy balance for this unsteady 1D system is

$$\frac{\partial T}{\partial t} = a\frac{\partial^2 T}{\partial z^2}. \qquad (3)$$

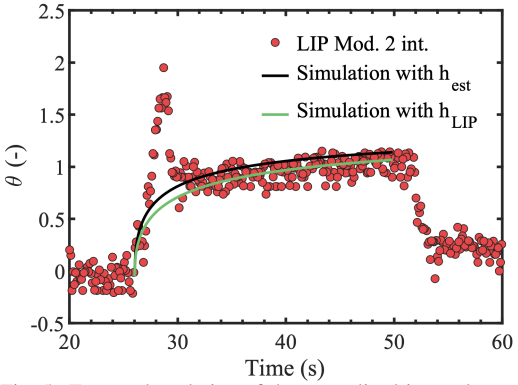

Fig. 5: Temporal evolution of the normalized internal surface temperature of the silica window in the 2nd module by LIP at WRP48 operating point. Simulation of this evolution with the semi-infinite medium model with an estimated convection coefficient (h_{est}) and found after an iterative procedure (h_{LIP}).

$T(z = 0, t)$ corresponds to the internal face temperature and $T(z = e, t)$ to the external face temperature. The initial and boundary conditions are

$$\begin{cases} T(z, t = 0) = T_i \\ T(\infty, t) = T_i \\ -\lambda\frac{\partial T(z=0,t)}{\partial z} = h\left[T_\infty - T(z = 0, t)\right]. \end{cases} \qquad (4)$$

T_i is the initial temperature of the window and is taken from LIP measurements before the beginning of the hot fire test. T_∞ is the temperature of the gas phase imposing convection and is taken from the thermocouples values (S4), corrected with the first estimation of the convection coefficient h_{est}. It is assumed that the gas temperature in the 2nd visualization module is equivalent to the one in the thermocouple module, 50 mm downstream. $t = 0$ is translated at $t = 26$ s on the LIP measurement time-line. With a variable change and the use of Laplace transform, the solution is

$$\frac{T-T_\infty}{T_i-T_\infty} = \mathrm{erf}\left(\frac{z}{2\sqrt{at}}\right) + \exp\left(\frac{hz}{\lambda} + \frac{ah^2t}{\lambda^2}\right)\mathrm{erfc}\left(\frac{z}{2\sqrt{at}} + \frac{h\sqrt{at}}{\lambda}\right), \qquad (5)$$

with $\mathrm{erf}(x)$ the Gauss error function and $\mathrm{erfc}(x) = 1 - \mathrm{erf}(x)$ the complementary error function.

The temperature peak is not modeled, so that temperatures can only be compared after $t = 32$ s. Figure 5 shows the result at $z = 0$ with the estimated value of the convection coefficient $h = h_{est} = 736\,\mathrm{W{\cdot}m^{-2}{\cdot}K^{-1}}$ applied for the silica window at WRP48 operating point. There is a good agreement between the measurements and the model, thereby confirming the hypothesis of the semi-infinite medium and a very good first estimation of the convection coefficient.

Based on these observations, it is possible to determine the convection coefficient by finding the best

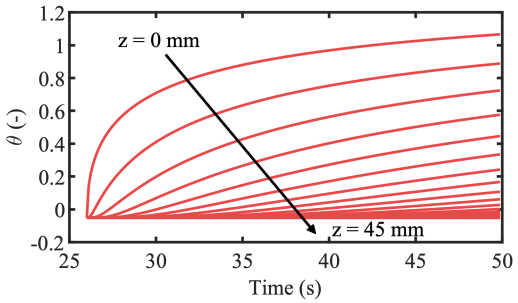

Fig. 6: Temporal evolution of the normalized temperatures inside the silica window in the 2nd module with a 1 mm step. Simulations using the semi-infinite medium model with $h = h_{LIP} = 564\,\mathrm{W{\cdot}m^{-2}{\cdot}K^{-1}}$ at WRP48 operating point.

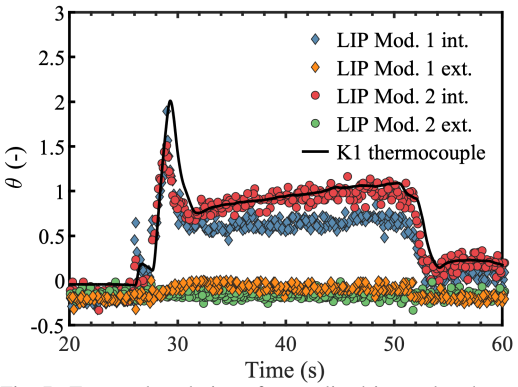

Fig. 7: Temporal evolution of normalized internal and external surface temperatures of silica windows in the 1st and 2nd modules and measured by K1 thermocouple at NRP48 operating point.

agreement between the temperature given by the model at $z = 0$ and the LIP measurements. A straightforward least mean square algorithm is implemented for this purpose. An iterative procedure is followed. For each value of the convection transfer found with the least mean square algorithm, the temperature given by the thermocouples are corrected thanks to equation 2 to reevaluate T_∞. The best value $h_{LIP} = 564\,\mathrm{W{\cdot}m^{-2}{\cdot}K^{-1}}$ is finally obtained after four iterations at WRP48 operating point. This final value is used to correct the thermocouple measurements, the temperature difference being 20 K at $t = 40$ s. The simulated temperature is plotted in figure 5, showing an even better agreement. The difference between the estimated value of the convection coefficient ($h_{est} = 736\,\mathrm{W{\cdot}m^{-2}{\cdot}K^{-1}}$) and the one found with LIP measurements ($h_{LIP} = 564\,\mathrm{W{\cdot}m^{-2}{\cdot}K^{-1}}$) probably comes from the estimation of the Reynolds and Prandtl numbers at an uncorrected value of the gas temperature and from the hypothesis that methane is the main component of the burnt gases.

The temperature determined with this model can be considered as a moving average of the measured temperature. The dispersion of LIP measurements around this temperature comes from a combination of two phenomena. On the one hand, one must consider the uncertainty associated with single-shot measurements previously estimated at ± 30 K. On the other hand, the surface temperature can fluctuate in time. Convection is the predominant thermal transfer and fixes the surface temperature, and the flow is highly turbulent. However, the relatively slow acquisition rate of LIP spectra (10 Hz) limits observable phenomena at 5 Hz (Shannon's principle). While thermocouples are acquired at a higher rate (100 Hz), their longer response time of a few hundred milliseconds limits the measurement of rapid fluctuations at a few hertz (2-3 Hz) too. In conclusion of this brief analysis, these fluctuations may have a physical meaning, but it remains challenging to interpret their amplitude.

Applying this value of the convection coefficient with the thermal properties of the blind window gives an average residual of $\sim$46 K, the model underestimating the temperature compared to the LIP measurements. The thermal properties taken for stainless steel 314 could slightly differ from the actual ones of the blind window due to repetitive test cycles through the years. In contrast, silica windows were brand new for this test campaign.

The temperature inside the silica window can finally be determined at any depth with the determined value h_{LIP}. It is plotted in figure 6 at WRP48 operating point. The temperature hardly increases after 10 mm as expected with the model and due to the very low diffusivity and conductivity of silica.

3.2.3. Near the flame

A comparison of the silica window temperatures measured by LIP (internal and external faces) in the 1st and 2nd visualization modules at NRP48 operating point is highlighted in figure 7. The first difference comes from the increase of external face temperatures. The hypothesis of the semi-infinite medium model is thus no longer possible in the 1st module, and convection may not be the predominant phenomenon that fixes the surface temperature.

For the internal surfaces, the increase of temperature, and the main temperature peaks are identical. After $t = 32$ s, the temperature still rises downstream of the flame, whereas it is constant and lower near the flame. Note that the first temperature peak at ignition due to the torch is captured at $t = 26$ s. The LIP measurement in the 1st module is performed in an outer recirculation zone between the flame and the injection plate, which may be at a low temperature because of the injection of cryogenic propellants. In contact with the injection plate, the recirculating gas/liquid structures in this zone may be at lower temperatures and lower velocities than downstream of the flame in the 2nd visualization module. Indeed, a dense phase has been observed recirculating around the conic shape of the flame. This dense phase could originate from

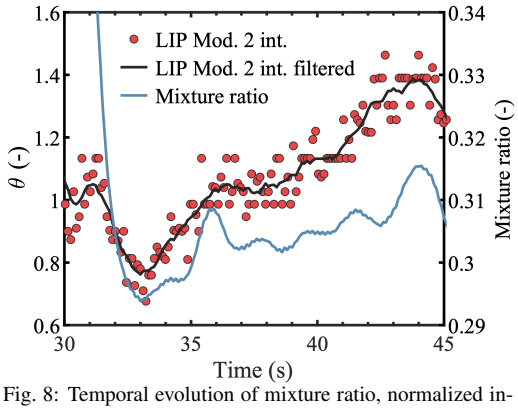

Fig. 8: Temporal evolution of mixture ratio, normalized instantaneous and filtered internal surface temperatures on the silica window in the 2nd module at NRP26 operating point.

the condensation of one or more species in the burnt gases. It would then result in a lower convection coefficient in the boundary of the internal LIP measurement and thus a lower surface temperature. These hypotheses should be verified with further measurements or numerical simulations.

3.2.4. During power modulation

Mass flow rates were slightly modulated for the operating point at 26 bar and without recess to reach different pressure levels during the same run. In the lower limit of operation of propellants valves, it results in an increasing and fluctuating mixture ratio around the targeted value of 0.3 as shown in figure 8. This test case of power modulation is well-suited for examining the ability of phosphor thermometry to track the associated temperature fluctuations. LIP measurements on the silica window in the 2nd module are thus plotted with the mixture ratio (figure 8). Most events are captured by LIP: the surface temperature increases or decreases with the mixture ratio with a slight delay. Very short and rapid variations may not be as well captured. As discussed before, the limitation comes from the acquisition rate at 10 Hz and not from the coating thermal equilibrium. Besides, the mixture ratio fluctuations only represent a deviation of less than 10% of the targeted value, but the thermal effects are still significant and well-captured by LIP.

4. Conclusions

Laser Induced Phosphorescence and the FSF method [15] have been used to simultaneously track the temperature evolution of five surfaces on the cryotechnic test bench MASCOTTE from ONERA operating in conditions representative of a gas generator.

In contrast to conventional sensors with slower response time, single-shot LIP measurements and the fast thermal equilibrium of the coating allowed the clear identification of the temperature peaks in the combustion chamber. Moreover, a classical heat transfer analysis showed the predominant effect of convection downstream of the flame.

From the measurements of internal and external surfaces of the silica window, a 1D semi-infinite medium model was applied, showing excellent prediction capacity. A comparison between this model and the measurements allowed an estimation of the convection coefficient in good agreement with the classical correlations used in turbulent convective flows. The temperature at any depth inside the window could be determined from this model, which is precious information when designing a test bench.

In the vicinity of the flame, LIP measurements showed lower surface temperatures in a recirculating zone. Besides, radiative transfers should play a more significant role here as the external temperature increases during hot fire tests.

Finally, dynamic phosphor thermometry showed the ability to track small power modulations. The acquisition rate could be increased to capture short events within the limit of overlapping decay due to the long lifetime of this phosphor at low temperatures. For very high repetition rate excitation, a shorter decay time phosphor should be used.

Acknowledgments

This work is part of an ongoing joint Ph.D. between EM2C laboratory and ONERA, co-piloted by CNES and ArianeGroup. The authors would like to thank the members of the MASCOTTE test bench and Nicolas Fdida from ONERA for their involvement during the experimental test campaign.

References

[1] A. Froehlich, M. Popp, G. Schmidt, D. Thelemann, Heat transfer characteristics of H2/O2-combustion chambers, AIAA, 1993.
[2] T. F. Guiberti, D. Durox, P. Scouflaire, T. Schuller, Impact of heat loss and hydrogen enrichment on the shape of confined swirling flames, Proc. Combust. Inst. 35 (2015) 1385–1392.
[3] R. Mercier, T. F. Guiberti, A. Chatelier, D. Durox, O. Gicquel, N. Darabiha, T. Schuller, B. Fiorina, Experimental and numerical investigation of the influence of thermal boundary conditions on premixed swirling flame stabilization, Combust. Flame 171 (2016) 42–58.
[4] S. Drogoul, From the failure to the success - The return to flight of the Ariane 5 ECA launcher, AIAA, 2005.
[5] L. Vingert, G. Ordonneau, N. Fdida, P. Grenard, A rocket engine under a magnifying glass, AerospaceLab 11 (2016) 15.
[6] M. D. Dramićanin, Trends in luminescence thermometry, J. Appl. Phys. 128 (2020) 040902.
[7] P. Nau, Z. Yin, K. P. Geigle, W. Meier, Wall temperature measurements at elevated pressures and high temperatures in sooting flames in a gas turbine model combustor, Appl. Phys. B 123 (2017) 279.
[8] A. Degenève, P. Jourdaine, C. Mirat, J. Caudal, R. Vicquelin, T. Schuller, Analysis of wall temperature and heat flux distributions in a swirled combustor powered

by a methane-air and a CO2-diluted oxyflame, Fuel 236 (2019) 1540–1547.
[9] C. M. Arndt, P. Nau, W. Meier, Characterization of wall temperature distributions in a gas turbine model combustor measured by 2D phosphor thermometry, Proc. Combust. Inst. 38 (2020).
[10] N. Fuhrmann, E. Baum, J. Brübach, A. Dreizler, High-speed phosphor thermometry, Rev. Sci. Instrum. 82 (10) (2011) 104903.
[11] C. Abram, B. Fond, A. L. Heyes, F. Beyrau, High-speed planar thermometry and velocimetry using thermographic phosphor particles, Appl. Phys. B 111 (2) (2013) 155–160.
[12] J. I. Eldridge, S. W. Allison, T. P. Jenkins, S. L. Gollub, C. A. Hall, D. G. Walker, Surface temperature measurements from a stator vane doublet in a turbine afterburner flame using a YAG:Tm thermographic phosphor, Meas. Sci. Technol. 27 (2016) 125205.
[13] H. Seyfried, G. Särner, A. Omrane, M. Richter, H. Schmidt, M. Aldén, Optical diagnostics for characterization of a full-size fighter-jet afterburner, ASME Turbo Expo, 2005.
[14] P. Nau, S. Görs, C. Arndt, B. Witzel, T. Endres, Wall temperature measurements in a full-scale gas turbine combustor test rig with fiber coupled phosphor thermometry, J. Turbomach. 143 (2020).
[15] V. Lechner, C. Betrancourt, C. Mirat, P. Scouflaire, S. Ducruix, Full spectrum fitting method: a new approach for instantaneous phosphor thermometry in harsh environments, Exp. Fluids 63 (7) (2022) 110.
[16] F. A. Abou Nada, C. Knappe, X. Xu, M. Richter, M. Aldén, Development of an automatic routine for calibration of thermographic phosphors, Meas. Sci. Technol. 25 (2) (2014) 025201.
[17] C. Knappe, M. Algotsson, P. Andersson, M. Richter, M. Tunér, B. Johansson, M. Aldén, Thickness dependent variations in surface phosphor thermometry during transient combustion in an HCCI engine, Combust. Flame 160 (2013) 1466–1475.
[18] B. Atakan, D. Roskosch, Thermographic phosphor thermometry in transient combustion: a theoretical study of heat transfer and accuracy, Proc. Combust. Inst. 34 (2013) 3603–3610.
[19] C. C. Pilgrim, J. P. Feist, A. L. Heyes, On the effect of temperature gradients and coating translucence on the accuracy of phosphor thermometry, Meas. Sci. Technol. 24 (10) (2013) 105201.